

Gaseous Dynamical Friction: A Challenge to Modern Hydrodynamical Schemes

B. Morton,¹★ S. Khochfar,¹ J. Oñorbe,²

¹*Institute for Astronomy, Royal Observatory, Edinburgh EH9 3HJ, UK*

²*Facultad de Física, Universidad de Sevilla, Sevilla, Spain*

Accepted XXX. Received YYY; in original form ZZZ

ABSTRACT

The process of momentum and energy transfer from a massive body moving through a background medium, known as dynamical friction (DF), is key to our understanding of many astrophysical systems. We present a series of high-resolution simulations of gaseous DF using Lagrangian hydrodynamics solvers, in the state-of-the-art multi-physics code, GIZMO. The numerical setup is chosen to allow direct comparison to analytic predictions for DF in the range of Mach $0.2 \leq \mathcal{M} \leq 3$. We investigate, in detail, the DF drag force, the radial structure of the wake, and their time evolution. The subsonic forces are shown to be well resolved, except at Mach numbers close to $\mathcal{M} = 1$. The supersonic cases, close to $\mathcal{M} = 1$, significantly under-shoot the predicted force. We find that for scenarios with $0.7 < \mathcal{M} < 2$, between 10% – 50% of the expected DF force is missing. The origin of this deficit is mostly related to the wake structure close to the perturber, where the density profile of the Mach cone face shows significant smoothing, which does not improve with time. The spherical expanding perturbation of the medium is captured well by the hydro-scheme, but it is the sharp density structure, at the transition from Mach cone to average density, that introduces the mismatch. However, we find a general improvement of the force deficit with time, though significant differences remain, in agreement with other studies. This is due to (1) the structure of the far field wake ($r \geq 4r_s$, with r_s as the gravitational smoothing scale) being reproduced well, and (2) the fraction of total drag from the far field wake increasing with time. Dark matter sub-haloes, in typical cosmological simulations, occupy parameters similar to those tested here, suggesting that the DF which these sub-haloes experience is significantly underestimated, and hence their merger rate. Dynamical friction is a relevant benchmark and should be included as one of the standard hydro test for astrophysical simulations, since it is critical to our understanding of many systems.

Key words: methods: numerical – hydrodynamics

1 INTRODUCTION

As a massive body moves through a region of lower mass bodies, gravitational interaction builds an over-density in the wake of the massive traveller. Momentum and energy are transferred, from this massive perturber, to the surrounding medium. This process is known as dynamical friction (DF), and is key to our understanding of the evolution of a number of astronomical systems, at very different mass and length scales, from galaxy clusters, to planets. Theoretical work, for purely collisionless media, was started decades ago (Chandrasekhar 1943). DF drives processes within structures from galaxy clusters (El-Zant et al. 2004; Kim et al. 2005; Adhikari et al. 2016), to satellite galaxies orbiting within their host halo (Zhao 2004; Fujii et al. 2006; Ogiya & Burkert 2016), super-massive black hole formation (Beckmann et al. 2018), compact object binaries and

mergers (Just et al. 2010; Dosopoulou & Antonini 2017; Tagawa et al. 2018), and planets within disks (Teysandier et al. 2012).

In the case of galaxy clusters, DF plays a key role in driving the accretion of substructure. Hierarchical collapse, within the standard Λ CDM cosmological model, predicts the presence of large numbers of low mass sub-haloes within higher mass hosts. The number density of satellites found in simulations follows a power law, with a slope of approximately -2, predicting a steep increase in the number density of satellites going to lower masses (Springel et al. 2008). These structures will experience both collisionless and gaseous DF, as they move within extended dark matter (DM) and circum-galactic medium (CGM) structure of the host. DF provides a mechanism by which they can shed angular momentum and energy, allowing them to merge with the central structure (Boylan-Kolchin et al. 2008; Khochfar & Ostriker 2008). In this way, DF drives the build-up of structure in a cold dark matter (CDM) cosmology. These mergers are a key driver of the evolution of galaxies, providing fuel for star

★ E-mail: morton@roe.ac.uk

formation and disrupting galactic structures (Barnes & Hernquist 1996; Beckman et al. 2008; Robaina et al. 2010; Khochfar et al. 2011; Somerville & Davé 2015). Gaseous DF is particularly pronounced at high redshifts, where halo gas mass fractions are highest (Daddi et al. 2010; Tacconi et al. 2010). The exact number, and spatial distribution, of DM sub-structures varies with different cosmological models. Large scale cosmological simulations are a key tool in testing these models, and the comparison of simulated and observed DM substructure is currently a key challenge for Λ CDM (Weisz & Boylan-Kolchin 2019).

The structure of the wake behind a perturber can be separated into two distinct contributions, one from a collisionless medium, such as background stars or dark matter, and one from a collisional medium, typically a baryonic gas. The additional pressure forces present in collisional media result in significant differences in the retarding drag force, when compared to the collisionless case (Ostriker 1999). This is most pronounced for Mach numbers close to $\mathcal{M} = 1$, where the combination of perturber mass and extent produce a wake that remains in the linear regime¹. As the scenario becomes increasingly non-linear, the gaseous DF drag force decreases (Kim & Kim 2009) (referred to as KK09 when mentioned directly). The complex structure of the gravitationally induced wake has been studied previously using both analytic (Just & Kegel 1990; Ostriker 1999; Namouni 2010) and numerical techniques (Sánchez-Salcedo & Brandenburg 1999, 2001; Kim & Kim 2007; Kim & Kim 2009; Bernal & Sánchez-Salcedo 2013). Bernal & Sánchez-Salcedo (2013) will be referred to as BS13 when directly mentioned in the text.

The analytic collisionless solution is found by calculating a sum of two body interactions, integrated over all time, between the perturber and particles that make up an infinite background medium (Chandrasekhar 1943). The analytical solution to the collisional case can be obtained in the linear regime, producing an approximation of the structure of the wake using linear perturbation theory (Just & Kegel 1990; Ostriker 1999). Within this linear approximation, the collisional drag force is significantly higher for perturbers moving with Mach numbers $0.7 < \mathcal{M} < 2$. A similar trend is also seen, in numerical simulations, for low mass, extended, perturbers (Sánchez-Salcedo & Brandenburg 1999; Kim & Kim 2009; Bernal & Sánchez-Salcedo 2013). Importantly, however, these works show the force from the wake is only accurately predicted under certain conditions. The force is found by integrating over the density distribution, which requires some lower limit r_{\min} , since the analytic solution diverges as radius $r \rightarrow 0$. These works utilise fitted values for r_{\min} , tuned to produce the expected force. Since r_{\min} sets the distance, from the perturber, from which the force integration is performed, it plays a crucial role when it comes to comparing numerical results to the analytic prediction. This element of the analysis is discussed in greater detail in Section 2.2. The analytic prescription can be extended numerically for more extreme mass perturbers, where large regions of the wake are no longer described by the linear wake (Kim & Kim 2009; Bernal & Sánchez-Salcedo 2013). The simulation work, in this regime, does not produce a clear picture of what the prediction for the non-linear wake should be.

More complex scenarios, such as those that include more physical processes, have also been studied, such as rigid perturbers that experience both gravitational drag, and the drag from physical collisions with the surrounding medium (Thun et al. 2016), as well as

perturbers on orbital trajectories (Sánchez-Salcedo & Brandenburg 2001; Kim & Kim 2007), and the effect of radiative feedback from an accreting black hole on the drag force (Toyouchi et al. 2020).

Despite the studies mentioned above, the ability of modern cosmological simulation codes to accurately capture the effects of gaseous DF, in its full cosmological context, has not been studied in detail. Capturing the effects of DF requires modelling the hydrodynamic response, as well as the purely gravitational effects. The nature of the hydrodynamic problem makes it difficult for traditional hydro solvers to model accurately (Tittley et al. 2001). The extended gaseous structure is highly unstructured, a challenge for Eulerian grid-based methods. Lagrangian particle-based methods, such as SPH (Gingold & Monaghan 1977), can better handle irregular density structures, but are less accurate at handling hydrodynamic instabilities (Agertz et al. 2007). In the last decade, a new hybrid class of methods have been developed, utilizing moving unstructured mesh approaches, which attempt to merge the advantages of the two. They aim to provide the instability and shock capturing efficiency of the grid-based methods with the natural resolution adaptation of the particle methods. Within astrophysics, these methods are still relatively new, although a number of established codes have emerged (Springel 2010; Duffell & MacFadyen 2011; Hopkins 2015; Duffell 2016; Springel et al. 2020). These have been shown to be generally competitive with the established multi-physics simulation codes (Wadsley et al. 2004; Springel 2005; Bryan et al. 2014; Gonnet 2014; Menon et al. 2015; Wadsley et al. 2017). They are ideal for studying the effects of DF, but little work has been done on this with these modern codes.

The impact of DF is a topic of significant ongoing study, in many different scenarios. Many of these works apply the DF drag force as an external source of momentum transfer, or apply the analytic treatment as a semi-analytic model, as opposed to self consistently producing the drag force by directly modelling formation of the density perturbation. This can be in the context of simulating massive black hole seed migration (Ma et al. 2021), the regularisation of stellar disc orbits (Bonetti et al. 2020), or the impact of DF from galaxy bars (Bortolas et al. 2021), to name some examples. For these works to be accurate, and for comparisons to be made between these results and more complete simulations, it is crucial that we understand how DF is resolved by modern simulation codes.

In this work we present a set of idealised, state of the art, three-dimensional gravo-hydrodynamic simulations of massive Plummer spheres, embedded within a uniform region of adiabatic gas moving with some velocity. In Section 2 we summarise the relevant analytic predictions, and their numerical non-linear extensions. Section 3 describes the numerical setup that we use, and 4 contains our results, showing the predicted wake, the force across a range of Mach numbers, and the time evolution of the force. In Section 5 we discuss these results, and examine the implication of our findings for dynamical friction experienced by dark matter sub-haloes in a cosmological context.

2 ANALYTIC SOLUTION TO DYNAMICAL FRICTION IN GASEOUS MEDIA

In contrast to dynamical friction in a collision-less medium, pressure gradients within a gaseous medium introduce additional forces on the evolving gas. These forces lead to the formation of structure within the over-dense wake. The time dependent form of this structure can be derived using linear perturbation theory to model the density perturbation as an expanding density wave (Ostriker 1999).

¹ Here the linear regime refers to wakes where the over-density factor is less than one throughout the wake.

2.1 Linear Wake

Using linear perturbation theory, [Ostriker \(1999\)](#)² produced an analytic prediction for the DF force felt by a point mass perturber M_p , moving at constant velocity V_0 in the z -direction through an infinite uniform density ρ_0 gaseous medium, where the gas has no self gravity. This medium has sound speed c_s , so the perturber moves with Mach number $\mathcal{M} \equiv V_0/c_s$. An analytic prescription for the density distribution of the induced wake, $\rho = \rho_0(1 + \alpha)$, results, described by the over-density $\alpha(s, R, t)$, with

$$\alpha = \frac{GM_p/c_s^2}{[s^2 + R^2(1 - \mathcal{M}^2)]^{1/2}} \times \begin{cases} 1 & \text{if } R^2 + z^2 < (c_s t)^2 \\ 2 & \text{if } \mathcal{M} > 1, R^2 + z^2 > (c_s t)^2, s/R < \\ & -(\mathcal{M}^2 - 1)^{1/2}, z > (c_s t)^2 \\ 0 & \text{otherwise} \end{cases} \quad (1)$$

where $s = z - vt$ is the distance from the perturber along the direction of travel and R is the cylindrical radius. Formally, this distribution diverges as the spherical radius $r \rightarrow 0$. However, we can analyse the wake where $\alpha < 1$. This part of the wake is approximately defined by $r \gtrsim r_{\min}$ with $GM_p/c_s^2 \lesssim r_{\min} \lesssim (V_0 - c_s)t$. The lower limit ensures that all parts of the wake included in this analysis are within the linear regime, while the upper limit makes sure that the wake has reached beyond r_{\min} .

By integrating over this over-dense wake, from r_{\min} to the edge of the wake, using

$$F_{\text{DF}} = 2\pi GM_p \rho_0 \int \int R \frac{\alpha(t)s}{(s^2 + R^2)^{3/2}} ds dR, \quad (2)$$

the corresponding drag force from this wake takes the form

$$F_{\text{DF}} = -\frac{4\pi(GM_p)^2 \rho_0}{V_0^2} I. \quad (3)$$

The parameter I represents the integral over the over-density and is the factor by which the DF force differs from the purely collisionless case. It depends on the Mach number of the case, with

$$I_{\text{sub}} = \frac{1}{2} \ln \left(\frac{1 + \mathcal{M}}{1 - \mathcal{M}} \right) - \mathcal{M} \quad (4)$$

for the subsonic perturbers, and

$$I_{\text{super}} = \frac{1}{2} \ln \left(\frac{\mathcal{M} + 1}{\mathcal{M} - 1} \right) + \ln \left(\frac{\mathcal{M} - 1}{r_{\min}/c_s t} \right) \quad (5)$$

for the supersonic perturbers. The I parameter, as a function of Mach number, is shown in Figure 1. This result is only accurate when all regions of the wake included in the force calculation remain linear. In other words, this solution assumes $\alpha < 1$. The force predicted by this approach is greater than the equivalent collisionless force, for a range of Mach numbers $0 \lesssim \mathcal{M} \lesssim 3$, with the largest difference close to $\mathcal{M} = 1$, where the collisional prediction is undefined. We use the standard definitions for sub-sonic $v_0 < c_s$, $\mathcal{M} < 1$, and super-sonic $v_0 > c_s$, $\mathcal{M} > 1$, with the transition point at $v_0 = c_s$, $\mathcal{M} = 1$.

When this prediction is tested numerically, the condition for the wake to remain linear $\alpha < 1$ can be parameterised using the global dimensionless parameter, A . For

$$A = \frac{GM_p}{c_s^2 r_s}, \quad (6)$$

² See [Just & Kegel \(1990\)](#) for an alternative derivation.

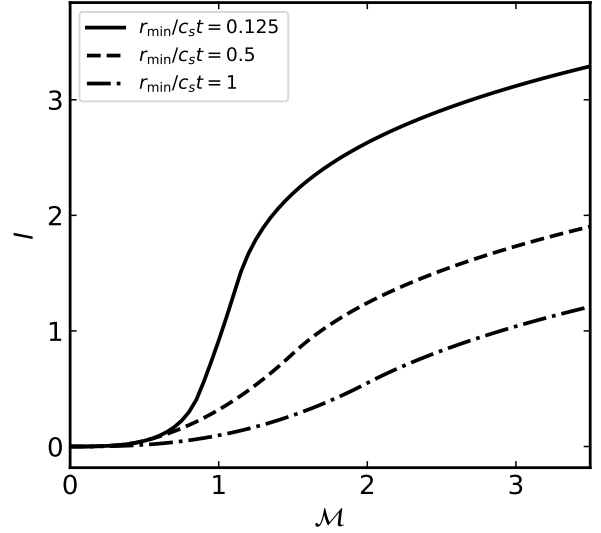


Figure 1. Value of integral I as a function of Mach number \mathcal{M} , for $r_{\min}/c_s t = 0.125, 0.5, 1$.

we require that $A < 1$ for the linear assumption to strictly hold. This estimates the density perturbation at approximately radius r_s , where r_s is the softening scale of the numerical potential (see Section 3.1). The A parameter effectively places a constraint on the physical scenarios that can be described by this prediction, since cases with very high mass perturbers, very small radii, or very large sound speeds, will violate the small A condition.

Any scenario can be completely described by two parameters: this A parameter, and the Mach number \mathcal{M} of the perturber moving through the gaseous background medium. The predicted force, given by Equations (3), (4) and (5), has been used to test numerical results, and they were found to match for suitably chosen A and r_{\min} ([Sánchez-Salcedo & Brandenburg 1999](#); [Kim & Kim 2009](#); [Bernal & Sánchez-Salcedo 2013](#)). As discussed in Section 1, these works find the forces match for when r_{\min} has certain values.

2.2 Choice of Minimum Radius

The net drag force is computed by integrating over the over-dense wake. An equivalent integration can be made over the output from a numerical simulation to produce the numerical drag force. The choice of r_{\min} , for these calculations, is usually determined by the condition that the numerical force integrated from r_{\min} to some maximum radius matches the analytic force integrated over the same range. This is in addition to the constraints on r_{\min} from the analytic considerations presented above.

For the numerical integration of the simulated wake, which performs the integral given in Equation 2, different authors have settled upon various values for r_{\min} . The value for r_{\min} is chosen such that the force from the wake matches the analytic prediction, making r_{\min} effectively a fitting parameter. Formally, the analytic force should match everywhere that the over-dense wake is linear, so where $r_{\min} \geq r_s$, but in practice the various numerical works find different r_{\min} fits. It should be noted that the softening scale r_s discussed here still refers to the scale length of the Plummer sphere used to represent the perturber, not the underlying gravitational softening of the simulation. We systematically investigate what radius can provide the equivalent fit for our numerical results, and discuss

how the detailed structure of the numerical wake brings this about, in Section 4.2.

It should also be noted that the match in force does not mean the numerical and analytic wakes necessarily have the same structure, just that the force matches. [Sánchez-Salcedo & Brandenburg \(1999\)](#) find that $r_{\min} = 2.25r_s$ accurately produces the predicted forces. BS13 estimate the value of r_{\min} using the position of the maximum density in the wake produced by a Plummer sphere, as opposed to a point mass, finding a value consistent with the [Sánchez-Salcedo & Brandenburg \(1999\)](#) result. KK09, on the other hand, find a Mach dependent prescription, with $r_{\min} = 0.35\mathcal{M}^{0.6}r_s$ providing the best fit for the force at $A = 0.01$, and argue that the difference between their result and previous ones is caused by differences in resolution and equation of state. BS13 address this suggestion, and find no difference in results between isothermal and adiabatic equations of state, or with resolution. They use the $r_{\min} = 2.25r_s$ fit, but also explore a Mach dependent fit, resulting in $r_{\min} = 1.5\mathcal{M}^{0.6}r_s$. BS13 conclude that it is only applicable at later times $t > 130t_c$ for supersonic perturbers. Both fits discussed by BS13 use a value significantly larger than that found by KK09, which has a dramatic effect on absolute value of the drag force from the wake. BS13 note that the KK09 fit can produce a force as much as a factor of two larger than their own. The value of r_{\min} is extremely important, when considering the drag force, as it determines over which radii the drag force is accurately reproduced and hence how much of the total drag force is recovered.

3 NUMERICAL METHOD

In this work we run a set of idealised, 3D, gravo-hydrodynamic simulations of DF, using the state-of-the-art multi-physics codes GIZMO ([Hopkins 2015](#)) and Gadget-4 ([Springel et al. 2020](#)), in order to compare them with the analytic predictions, and previous numerical results. In this section, we describe our numerical approximation of the idealised case for DF, the key parameters used in the code setup, and the initial conditions of the simulations.

3.1 Setup

The numerical setup is designed to closely replicate the assumptions made in the derivation of the analytic solution. The initial conditions have a uniform density ρ_0 adiabatic gas, moving with bulk velocity V_0 , in a 3D box with a fixed gravitational potential Φ from a massive perturber M_p . The bulk velocity has Mach number $\mathcal{M} = V_0/c_s$. The gas does not experience self gravity, and the boundaries of this box are periodic. The massive perturber has the form of a Plummer sphere ([Plummer 1911](#)), with potential

$$\Phi(r) = -\frac{GM_p}{(r^2 + r_s^2)^{\frac{1}{2}}}, \quad (7)$$

with mass M_p and softening r_s . This softening is analogous to the extent of the perturbing object. The simulation time is characterised by sound speed crossing time of this length $t_c = r_s/c_s$.

To reproduce the initial uniform density, we generate glass-like initial conditions (ICs) using WVTICs ([Donnert et al. 2017](#); [Arth et al. 2019](#)), which combines a weighted Voronoi mesh with a particle shuffling method to reproduce arbitrary density distributions with a set of SPH particles. The ICs created with this method were found to be superior to simple initial grids and random particle placements, minimising periodic oscillations in the net force

on the perturber, and reducing initial variation in the local density distribution.

The idealised setup is effectively scale free, characterised by A in Equation (6) and the Mach number \mathcal{M} . The A parameter sets the relationship between the perturber, from its mass and extent, and the medium, through the sound speed. In this context, the extent is taken to be equivalent to the softening scale of the potential. It should be noted that the A parameter is defined by this softening scale, and the lower limit of the force integral r_{\min} plays no role in defining the setup. Instead, the lower limit functions as a numerical fitting parameter, as discussed above. While we initially take $r_{\min} = r_s$, this is not strictly required by the derivation. We choose to show forces calculated using $r_{\min} = r_s$ for simplicity unless otherwise stated. We present radial break downs of the net force that show what r_{\min} would produce a good fit in Section 4.3.

The relative motion is captured by the Mach number. We run setups for a range of Mach numbers, exploring the regime where collisional DF differs most from collisionless DF, for $0.7 < \mathcal{M} < 2.0$. A range of A values was also explored, from far inside the linear regime ($A = 0.01$) through the transition regime ($A = 1$) and beyond, into the highly non-linear regime ($A = 10$). A number of different box sizes and resolutions were used. The different setups are summarised in Table 1. The size of the box L , and number of particles N , are both varied in certain runs. Varying the particle number is used to effectively test the convergence of our results with resolution.

To test the behaviour of the numerically modelled gas under different conditions, it is necessary to explore the scale free parameter space of A and Mach number. The setup is constrained by the periodic boundary conditions, setting an upper limit on how long the scenario can be run before the wake reaches the edge of the box, and so wraps around. This time is defined by the edge length of the box and the initial velocity of the gaseous background. A range of Mach numbers were probed, exploring the regime around the strongest gaseous signal at $\mathcal{M} = 1$. The majority of the boxes are run for $t = 15t_c$, with the larger boxes pushed to $t = 150t_c$. Each box was run until the wake reached close to the edge of the periodic box. If it were run longer, the edge of the over-dense wake would rap around. Larger boxes allow for longer runs, but at the cost of reduced mass resolution, critical to recovering the small over-densities in the wake structure. Our setup reaches $t = 15t_c$ in the standard runs, and the largest boxes reach $t = 150t_c$, while still retaining acceptable mass resolution.

3.2 Solvers

We investigate the differences in the numerical results for the Lagrangian meshless finite mass (GOMFM) ([Hopkins 2015](#)) and pressure-entropy smoothed particle hydrodynamics (GOPSPH) ([Hopkins 2013](#)) hydro-solvers. The GOMFM solver uses a state-of-the-art method that discretises the volume with a kernel function and solves the Riemann problem between the neighbouring particles, utilising a high order gradient estimator. The GOPSPH solver is an extension to the standard SPH formulation ([Gingold & Monaghan 1977](#)). It estimates pressure gradients using entropy rather than density, reducing inaccuracies at fluid interfaces, and the required number of kernel particles. The idealised DF problem has not been investigated in detail using these modern Lagrangian solvers, so our understanding of their detailed behaviour in this context is currently limited and provides a further test for the numerical accuracy of these schemes. We corroborate our results by comparing

Table 1. Details of all the simulation runs. Solvers refer to either the GIZMO (GO) or Gadget4 (G4) codes, using either the MFM or PSPH solvers. L is the length of the edge of the cube box in kilo-parsecs, N is the number of particles, and t_{final} the end time of the simulation, in units of sound speed crossing time t_c of the softening length r_s .

ID	Solver	L	N	\mathcal{M}	A	t_{final}
GM512M02A01	GOMFM	10	512	0.2	0.1	15
GM512M07A01	GOMFM	10	512	0.7	0.1	15
GM512M09A01	GOMFM	10	512	0.9	0.1	15
GM512M1A01	GOMFM	10	512	1.01	0.1	15
GM512M11A01	GOMFM	10	512	1.1	0.1	15
GM512M13A01	GOMFM	10	512	1.3	0.1	15
GM512M15A01	GOMFM	10	512	1.5	0.1	15
GM512M2A01	GOMFM	10	512	2	0.1	15
GM512M3A01	GOMFM	10	512	3	0.1	15
GM512M02A1	GOMFM	10	512	0.2	1	15
GM512M07A1	GOMFM	10	512	0.7	1	15
GM512M09A1	GOMFM	10	512	0.9	1	15
GM512M101A1	GOMFM	10	512	1.01	1	15
GM512M11A1	GOMFM	10	512	1.1	1	15
GM512M13A1	GOMFM	10	512	1.3	1	15
GM512M15A1	GOMFM	10	512	1.5	1	15
GM512M2A1	GOMFM	10	512	2	1	15
GM512M3A1	GOMFM	10	512	3	1	15
GM512M13A001	GOMFM	10	512	1.3	0.01	15
GM512M13A10	GOMFM	10	512	1.3	10	15
GP512M13A01	GOPSPH	10	512	1.3	0.1	15
GP512M13A1	GOPSPH	10	512	1.3	1	15
GM1024M13A01L	GOMFM	100	1024	1.3	0.1	150
GM1024M13A1L	GOMFM	100	1024	1.3	1	150
GM64M13A01	GOMFM	10	64	1.3	0.1	15
GM128M13A01	GOMFM	10	128	1.3	0.1	15
GM256M13A01	GOMFM	10	256	1.3	0.1	15
GM64M13A1	GOMFM	10	64	1.3	1	15
GM128M13A1	GOMFM	10	128	1.3	1	15
GM256M13A1	GOMFM	10	256	1.3	1	15
4P512M13A01	G4PSPH	10	512	1.3	0.1	15
4P512M13A1	G4PSPH	10	512	1.3	1	15

them to an independent implementation of the PSPH solver in the Gadget4 code (Springel et al. 2020), referred to here as G4PSPH.

4 RESULTS

In this section, we compare the numerical results from the simulations described above, with the analytic predictions. We primarily discuss the results with the GOMFM solver, unless otherwise stated. The analytic solution strictly holds for $A < 1$, and previous works have shown the predicted force can be recovered for $A \leq 1$, but only for certain values of the minimum radius of the force integral r_{min} suggesting that the wake at radii smaller than r_{min} is not well recovered (Kim & Kim 2009; Bernal & Sánchez-Salcedo 2013). We will use r_{min} , in the following, as a free parameter to adjust the range over which we compare the simulation with analytic predictions.

4.1 Force

The analytic prediction for the net gravitational force, from the wake, on the perturber is given by Equation (3). In the subsonic case, this solution to the integral holds for $r_{\text{min}} < (c_s - V_0)t$, which requires the wake is larger than the effective size of the perturber. For supersonic cases, the solution is found by assuming

$r_{\text{min}} < (V_0 - c_s)t$, which means that the lower limit of the integral is inside the cone section of the wake. A numerical integration of the analytic over-density α is used at times when these conditions were not satisfied. For instance, this would be when the cone part of the wake is entirely inside r_{min} , but the spherical part extends beyond r_{min} . This allows us to produce an accurate force for the analytic wake solution, no matter the limits of the integration. The equivalent force from the simulation outputs is calculated by direct force summation. The Newtonian gravitational force is calculated between each particle of mass M_{part} , and the massive perturber M_p . All particles within $r < r_{\text{min}}$ of the perturber are excluded from the calculation.

The force is dependent on the Mach number and time. In Figure 2, we show the variation in the numerical and analytic forces with Mach number for two sets of runs at $t = 15t_c$, one with $A = 0.1$ and the other with $A = 1$, showing results from runs GM512M02A01 to GM512M3A1. We see that both $A = 0.1$ and $A = 1$ show numerical forces less than the analytic prediction for supersonic cases, with up to 50% of the force missing close to $\mathcal{M} = 1$ for $A = 1$, and as much as 25% for $A = 0.1$. The subsonic setups, on the other hand, show good agreement at $\mathcal{M} \leq 0.7$, with some divergence at $\mathcal{M} = 0.9$. The $A = 0.1$ case shows smaller residuals (Figure 2, lower panel), while the $A = 1$ case is worse at all Mach numbers, excepting those with $\mathcal{M} < 0.7$. The $A = 1$ results show a force that is 25 – 50% below the predicted value, while the $A = 0.1$ forces are 10 – 25% lower than expected. The difference is most extreme in the supersonic regime close to $\mathcal{M} = 1$. The agreement therefore gets worse as the setups become less linear.

At larger Mach numbers $\mathcal{M} \geq 2$, the numerical results show significantly less force deficit, and so a better match with analytical predictions, than those close to $\mathcal{M} = 1$. The analytic force is also smaller, in this regime, so physical objects in this regime will experience less drag. We will therefore focus our analysis and discussion to $0.7 < \mathcal{M} < 2$, where the absolute and proportional differences are most pronounced.

The trend with linearity is also seen in Figure 3, where we show the evolution of the force with time at $\mathcal{M} = 1.3$ for $A = 0.01$, $A = 0.1$, $A = 1$ and $A = 10$. These results come from runs GM512M13A001, GM512M13A01, GM512M13A1 and GM512M13A10. The most non-linear case $A = 10$ shows extreme deviation from the linear prediction, with 75% of the expected force missing. This plot also demonstrates the increase in variation of the force as the ratio of particle mass to perturber mass increases (see Appendix A). This effectively limits the A values that can be tested. The A parameter is reduced in these scenarios by reducing the mass of the perturber, so the perturber for $A = 0.01$ has $1/10^{\text{th}}$ the mass of the $A = 0.1$ perturber. The time evolution of the force in each case shows that the solution differs from the analytic prediction at all times with moderate improvement for the case deep in the linear regime with $A \leq 0.1$. We see that the $A = 0.01$ and $A = 0.1$ cases have effectively converged, showing that moving deeper into the linear regime will not change the results and we will use $A = 0.1$ as our fiducial setup.

When comparing to the analytic prediction, the choice of r_{min} is limited by the requirement that the prediction only holds for a wake where the over-density is linear. We chose first to calculate results for $r_{\text{min}} = r_s$, as shown in Figures 2 and 3, where our choice of A means the wake should remain in the linear regime for all parts included in the integration ($A \leq 1$). It is clear that parts of this numerical wake deviate from the analytic prediction. We find that the force from $r_{\text{min}} = 4r_s$ matches the analytic prediction in the $A = 0.1$ case, and from $r_{\text{min}} = 8r_s$ with $A = 1$. When $r_{\text{min}} = 4r_s$,

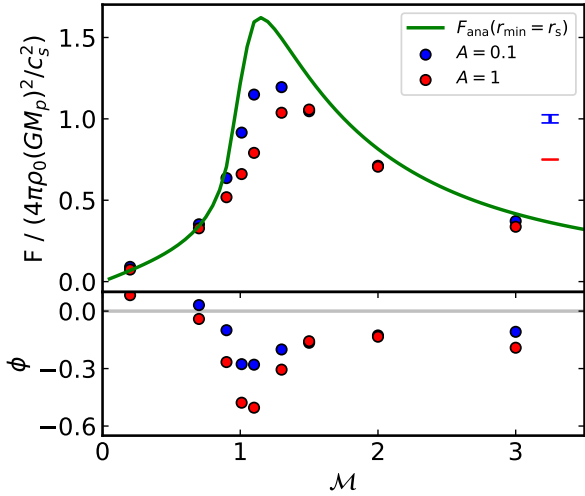


Figure 2. *Upper Panel:* Dimensionless force from numerically induced wakes across a range of Mach numbers, at $t = 15t_c$. We show the numerical results (dots) and the corresponding analytic prediction (green line). The error bars show an estimate of the intrinsic error in the force for each case (see Appendix A). The force is well recovered in the subsonic regime, but diverges significantly for supersonic cases. The $A = 0.1$ setup provides a better match than the $A = 1.0$ case. The error in the $A = 1$ is higher, but the trend in the results is still clear. *Lower Panel:* Residual between the numerical and analytic results $\phi = (F_{\text{num}} - F_{\text{ana}})/F_{\text{ana}}$.

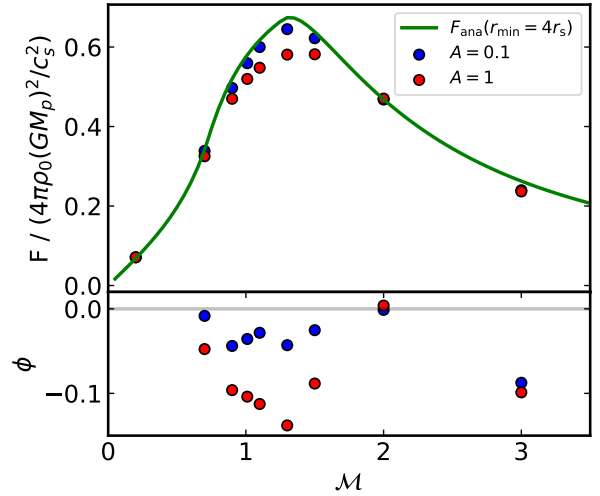


Figure 4. *Upper Panel:* Dimensionless force from numerically induced wakes across a range of Mach numbers, at $t = 15t_c$. We show the numerical results (dots) and the corresponding analytic prediction (lines) for $r_{\text{min}} = 4r_s$. Error bars are not shown for these results, as the intrinsic errors are negligible compared to the absolute forces for this r_{min} . The $A = 0.1$ results now show fairly good agreement at all mach numbers, with residuals at the few percent level. The $A = 1$ results still show significant difference, of order 20%. *Lower Panel:* Residual between the numerical and analytic results $\phi = (F_{\text{num}} - F_{\text{ana}})/F_{\text{ana}}$.

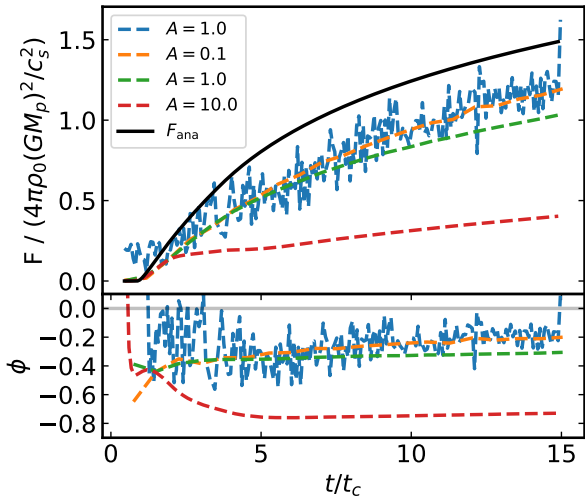


Figure 3. *Upper Panel:* Time evolution of the dimensionless force for $A = 0.01$, $A = 0.1$, $A = 1$ and $A = 10$. The highly nonlinear case diverges early, while the transition case ($A = 1$) is a better match, but still differs from the strictly linear cases. *Lower Panel:* Residual between the numerical and analytic results $\phi = (F_{\text{num}} - F_{\text{ana}})/F_{\text{ana}}$.

the numerical force from the $A = 0.1$ results are within 5% of the expected value, while the $A = 1$ forces are missing 10% of the analytic force. For $r_{\text{min}} = 8r_s$, forces from both $A = 0.1$ and $A = 1$ are within 5% of the prediction. The forces produced when using these fits are shown in Figures 4 and 5 respectively. The fits are focused on the Mach range of most interest $0.7 < \mathcal{M} < 2$. The trend in the fit for the results outside this range is less well defined. The details of the variation of the residual with r_{min} will be covered in Section 4.5.

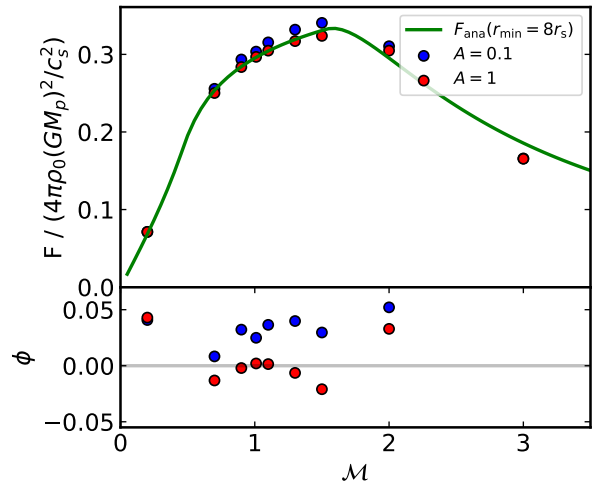


Figure 5. *Upper Panel:* Dimensionless force from numerically induced wakes across a range of Mach numbers, at $t = 15t_c$. We show the numerical results (dots) and the corresponding analytic prediction (lines) for $r_{\text{min}} = 8r_s$. Once again the intrinsic error is negligible. Both $A = 0.1$ and $A = 1$ results show agreement within 5%, with some numerical results now above the analytic prediction. *Lower Panel:* Residual between the numerical and analytic results $\phi = (F_{\text{num}} - F_{\text{ana}})/F_{\text{ana}}$.

It is not clear, from the force calculation alone, what is causing the mismatch in force within $4r_s$ ($A = 0.1$), or $8r_s$ ($A = 1$). In the next sub-section, we show that the far-field wake beyond this radius matches the analytic prediction well, but the structure within this radius diverges significantly from the prediction.

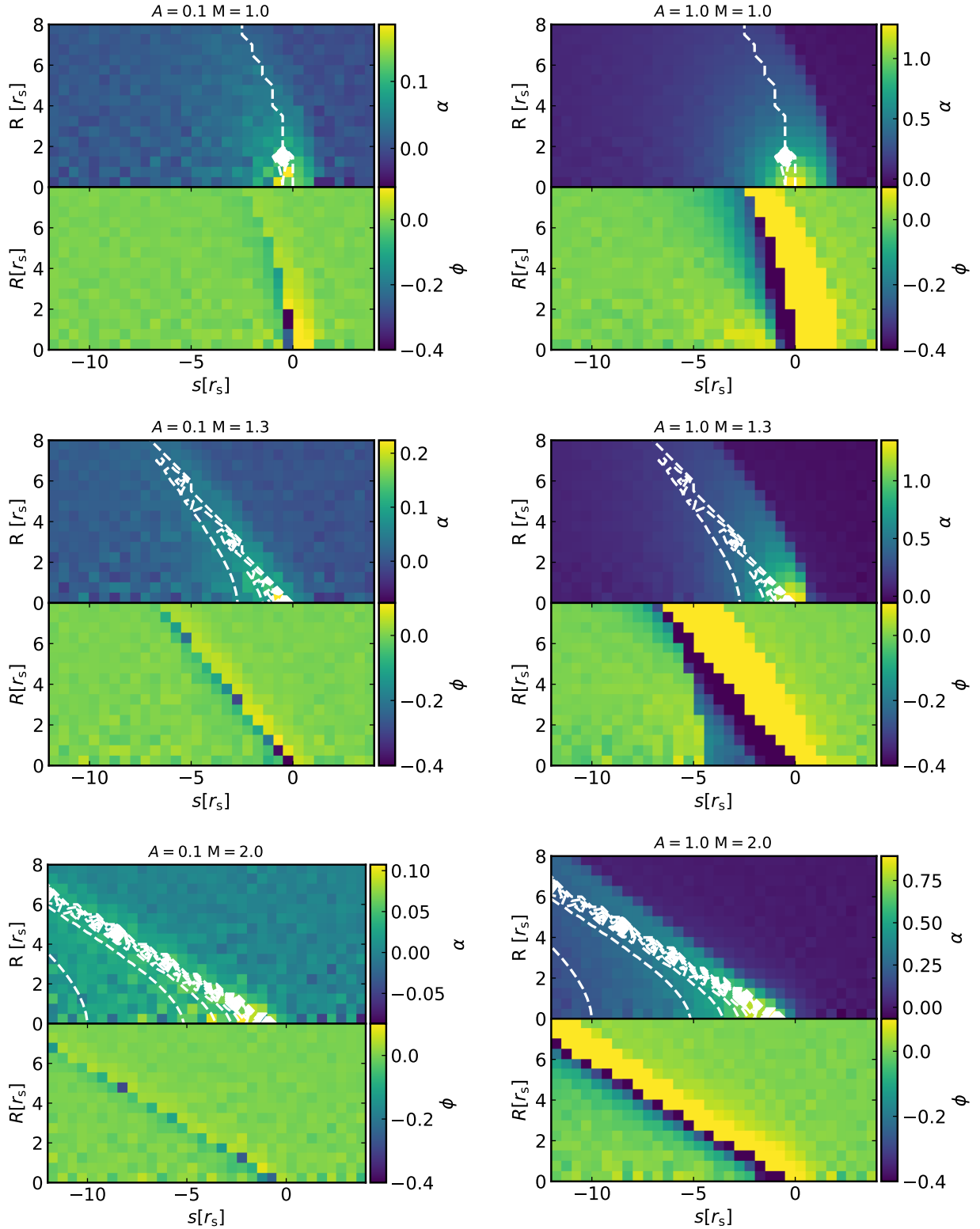


Figure 6. Zoomed view of over-density for $A = 0.1$ (left column), and $A = 1$ (right column), across $\mathcal{M} = 1.01, 1.3, 1.5$, at $t = 15t_c$. The upper part of each panel showing the numerical over-density α_{num} in the colour, and the analytic prediction for the over-density α_{ana} as white dashed contours. We see the development of a bow shock like structure ahead of the perturber. This structure extends further forward in the $A = 1$ case, and is denser. In the $A = 0.1$ case, the effect is much smaller, though still present. The structure shrinks at higher mach numbers, with the biggest divergence close to $\mathcal{M} = 1$ in both cases. The difference between these distributions $\phi = \alpha_{\text{num}} - \alpha_{\text{ana}}$ are shown in the lower part of each panel.

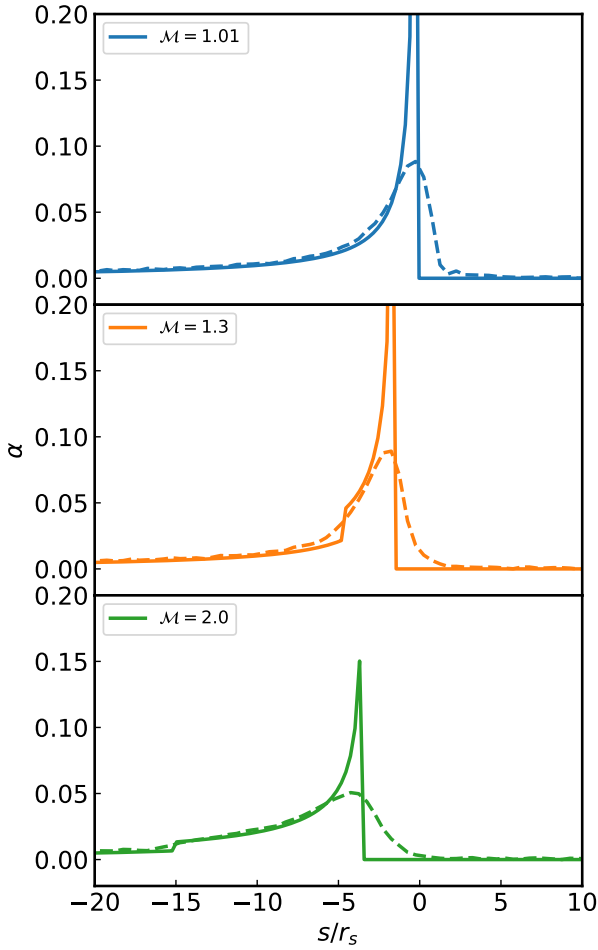


Figure 7. Profile of over-density α along a line of constant $R = 2r_s$, for $A = 0.1$ at $t = 15t_c$, with $\mathcal{M} = 1.01$ (top), $\mathcal{M} = 1.3$ (middle), and $\mathcal{M} = 2$ (bottom). The profiles are from the same results as those shown in the left column of Figure 6. Solid lines show the analytic solution, dashed lines show the numerical result.

4.2 Wake

To understand the differences between the analytic and numerical results, and why the numerical results are systematically missing 10 – 50% of the expected force, we directly compare the numerical density distribution to the analytic prediction for the form of the wake, given by α in equation (1). The numerical over-density is found by binning the particles into (s, R) cylindrical bins, then dividing the density in that bin by the initial background density and subtracting one. Here s is the distance from the perturber along the direction of travel, and R is the cylindrical radius away from this axis. In Figure 6, we show the structure of the numerical over-density, with contours showing the analytic prediction (white dashed lines), for three Mach numbers, with both $A = 0.1$ (left column) and $A = 1$ (right column). The residual (here the difference between numerical and analytic results) shows us that the Mach cone structure is the main source of error. The sharpness of the density peak in the cone has been softened, with the density smeared out into a wider profile. The peak in the cone over-density is too small, and extends too far forward. The smearing of the profile is on a scale larger than the spatial resolution of the simulation l , with the profile spread over approximately $20l$. These features are clearly seen in Figure

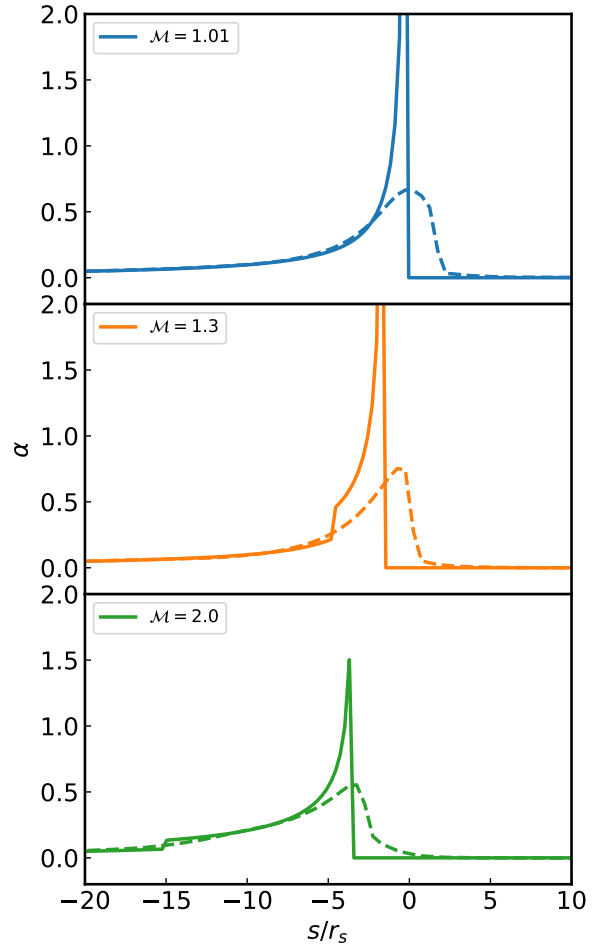


Figure 8. Profile of over-density α along a line of constant $R = 2r_s$, for $A = 1$ at $t = 15t_c$, with $\mathcal{M} = 1.01$ (top), $\mathcal{M} = 1.3$ (middle), and $\mathcal{M} = 2$ (bottom). The profiles are from the same results as those shown in the right column of Figure 6. Solid lines show the analytic solution, dashed lines show the numerical result.

7, where we show the over-density α on a line of constant $R = 2r_s$, for $A = 0.1$, and the equivalent for $A = 1$ shown in Figure 8. Each Mach number is shown in a different panel, from top to bottom $\mathcal{M} = 1.01, 1.3, 2$, with the solid line showing the analytic solution, and the dashed line showing the numerical result. The smeared potential is reminiscent of the bow shock structure shown to form for non-linear cases, but now in the linear regime. It is not identical to the non-linear results found by previous works, however, as it does not show any more complex structure growth, such as detached vortices (Kim & Kim 2009; Bernal & Sánchez-Salcedo 2013).

The bow-like structure is most pronounced for $\mathcal{M} = 1.01$, for both $A = 0.1$ and $A = 1$, and gradually diminishes as Mach number increases. The smearing out of the density profile across the cone front is present at all Mach numbers with $A = 1$, although it does reduce in width. The $A = 0.1$ profile has the smearing all but vanishing at $\mathcal{M} = 2$. The structure is generally well matched at large radii from the perturber, where the over-density is very small, but the cone is only well recovered beyond $s = 8r_s$ behind the perturber. For all Mach numbers, the less linear setup shows a higher value in its over-density, as expected for a higher mass perturber. The shock

also extends further forward of the predicted structure for the less linear case.

In the $A = 1$, $M = 1.3$ case (middle right), we see that the over-density in the part of the wake within the cone is lower than the predicted value, while the over-density on the spherical part of the wake is well recovered. No equivalent pattern is seen for $A = 0.1$. This shows again that it is not just the cone front that is not replicated, but also the profile behind the edge of the cone. At $A = 1$, $M = 2$, the profile is evenly smeared either side of the predicted front, while the over-density further within the cone is well recovered.

These differences in structure fit with the net forces that we calculate for the different Mach numbers. The largest divergence in force is close to $M = 1$, where we see the largest over-density ahead of the perturber and the poor recovery of the shock front itself, while at large Mach numbers the force is a better match, with the small difference likely explained by the smoothing out of the cone profile. In the intermediate case, we also see significant divergence, once again explained by both the bow-like structure and the smearing out of the cone profile. The spherical parts of the wakes are in general well recovered. Additionally, there is less fluctuation in the density of the wake, in the less linear $A = 1$ case, as the over-density is greater, and so contains more particles.

We can break down the contribution to the force into spherical shells to better understand how the different parts of the structure are contributing to the force. This is simply done by performing the direct force summation for particles within a given radius range of the perturber. The results for the $A = 0.1$ scenario are shown in Figure 9. This shows the numerical and analytic contributions to the force, as a fraction of the analytic force from the whole wake; i.e. from $r_{\min} = r_s$ to $r_{\max} = 2r_s$. We use radial bins of $r_{\min} = r_s$ to $r_{\max} = 2r_s$, $r_{\min} = 2r_s$ to $r_{\max} = 4r_s$, $r_{\min} = 4r_s$ to $r_{\max} = 8r_s$, and $r_{\min} = 8r_s$ to $r_{\max} = 12r_s$. We see that the force matches to within 5% at radii beyond $r = 4r_s$. Inside this radius, the force is poorly recovered at all times, with the majority of the difference coming from $r = r_s$ to $2r_s$. In this inner region, more than 20% of the force is missing. This fits with what we see in the numerical wake, with the bow-like structure and shallower cone profile at the tip of the cone producing the mismatch, while as we move out in spherical shells, the contribution from the softened cone profile continues to have an effect. This diminishes as more of the force comes from the well resolved interior of the cone. The deviations from the analytic solution, at small radii, do not propagate to larger radii as the wake expands, but instead remain confined to the innermost $4r_s$ of the wake.

The corresponding result for the $A = 1$ case (Figure 10) shows a similar pattern, although in this case the force is only a good match beyond $r = 8r_s$. From $r = 8r_s$ outwards, the numerical force is within 5% of the analytic value for $A = 1$. The match in this radial bin is within 1% for $A = 0.1$. With $A = 1$, the fraction of missing force increases as we move inward from this radius, with 5–10% missing in the $r = 4r_s$ to $8r_s$ bin, 10–15% between $r = 2r_s$ to $4r_s$, and 20–50% between $r = 1r_s$ to $2r_s$. The fraction missing from each radial bin is larger than its $A = 0.1$ counterpart, showing us that the wake diverges more across the whole range. Once again, this fits with the differences in the bow-like structures we see in both numerical wakes. The more extended bow-like structure has an effect at greater radii, since it extends further forward. The interior of the cone is less well recovered, making the mismatch even larger. The far-field wake is well recovered, and we see this in the matching of the force for these larger radii.

In both cases, the force shows strong disagreement at very early

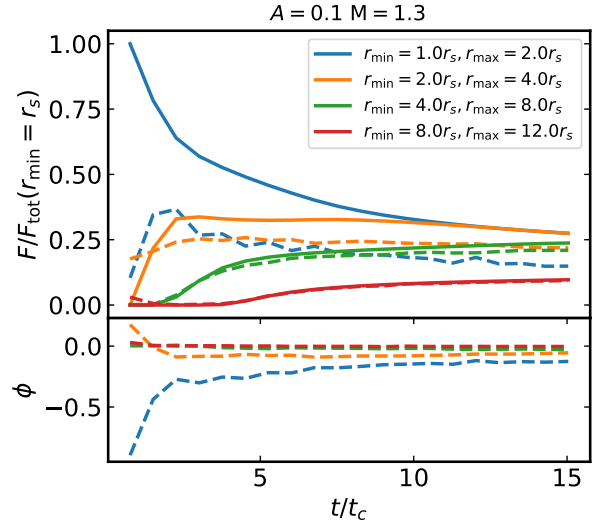


Figure 9. *Upper Panel:* Time evolution of the analytic (lines) and numerical (dashed lines) drag force contribution from radial bins for $A = 0.1$. The force is shown as a fraction of the total analytic force from the whole wake. The numerical and analytic forces match well outside $r = 4r_s$. The force deficit comes from inside this radius for this case. *Lower Panel:* Residual between numerical and analytic forces in that radial bin, as a fraction of the force from the whole wake at that time $\phi = (F_{\text{num}} - F_{\text{ana}})/F_{\text{ana,tot}}$. The residual has converged to a steady solution by $t = 15t_c$, showing the total force deficit of roughly 25% will remain for large times.

times, but reaches a quasi-steady value by $t = 10t_c$. At these early times, the whole force comes from the innermost bin, since the wake has not extended very far. As time continues, we would expect the total force mismatch to diminish, as the inner regions which make up most of the difference, contribute less of the total force. A higher fraction of the force comes from the far-field wake at larger times, which is well matched.

4.3 Long Term Evolution

So far we have shown results for only the first $15t_c$ of the evolution of the gravitationally induced wake. Previous works (Sánchez-Salcedo & Brandenburg 1999; Kim & Kim 2009), which find different fits for best matching r_{\min} , report results at many hundreds of crossing times. At these times the wake has reached scales hundreds of times the gravitational softening scale of the perturber. The results from the larger box are shown in Figure 11, using runs GM1024M13A01L and GM1024M13A1L. The intrinsic variation in the force is larger for these larger boxes, where $M_{\text{part}}/M_p = 8 \times 10^{-7}$ for $A = 0.1$ and $M_{\text{part}}/M_p = 8 \times 10^{-8}$ for $A = 1$ (see Appendix A). In summary of this variation, the discretisation of the gas by mass leads to some fluctuation in the net force on the perturber. This fluctuation is greater when the mass ratio of the particle to perturber is large, since a single particle can exert a greater force on the perturber. This effectively places some limits on the setups that can be feasibly run, since very large variation will prevent meaningful results being extracted from the simulation output.

The $A = 0.1$ case is close to being in approximate agreement, within its intrinsic variation, but still remains systematically offset below the analytic solution. There is still a deficit in the numerical force at these late times, when the wake is much larger, amounting to approximately 5%–10% missing in the $A = 0.1$ case, and

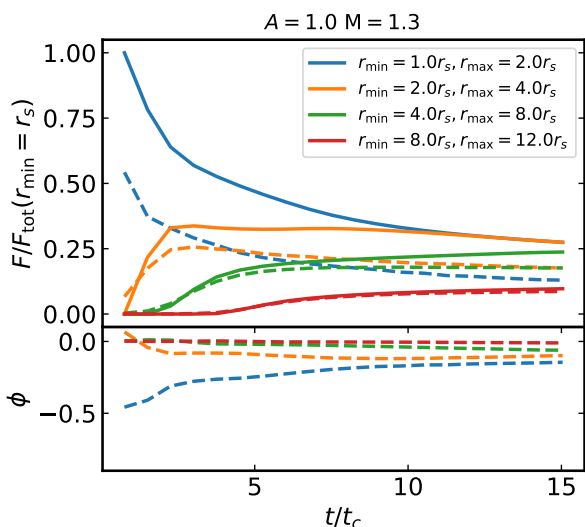


Figure 10. *Upper Panel:* Time evolution of the analytic (lines) and numerical (dashed lines) drag force contribution from radial bins for $A = 1$. The numerical and analytic forces match well outside $r = 8r_s$, so a larger region is producing the force deficit, when compared to the $A = 0.1$ case. *Lower Panel:* Residual between numerical and analytic forces in that radial bin, as a fraction of the force from the whole wake at that time $\phi = (F_{\text{num}} - F_{\text{ana}})/F_{\text{ana,tot}}$.

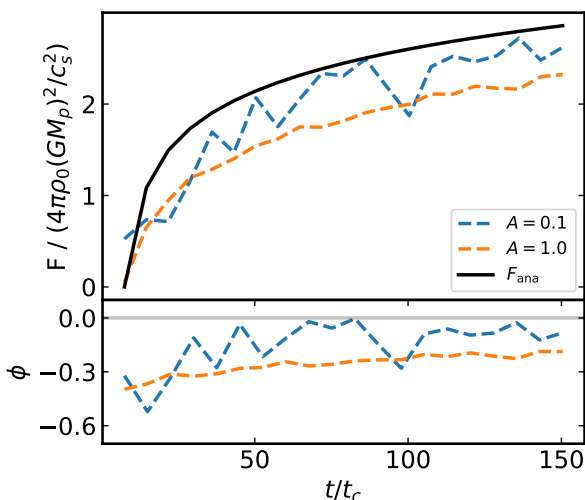


Figure 11. *Upper Panel:* Time evolution of the dimensionless force for $A = 0.1$ and $A = 1$ in the larger $L=100\text{kpc}$ box. The $A = 0.1$ case does not converge to the analytic solution in this longer time. *Lower Panel:* Residual between analytic and numerical results $\phi = (F_{\text{num}} - F_{\text{ana}})/F_{\text{ana}}$.

approximately 25% with $A = 1$. We do not see a significant change in the pattern observed for the results at $t = 15t_c$. While there is some suggestion that the difference in the $A = 0.1$ case may be reducing, it has not converged on the predicted force even at this late time. The force match from the inner radial bins does not improve significantly over this time. The contribution from this region, as a fraction of the total force from the whole wake, does decrease over time, but this process is very slow. The contribution from small radii remains large, since these regions are expected, and observed, to show the greatest over-density, and are, by definition, closest to the perturber. The key point, therefore, is that while the matching of

the force may improve slightly at late times, we find that this effect is small, and that the recovery of the force from the inner radial bins does not improve.

The results presented in Sections 4.1 to 4.3 show that we have a deficit in the expected force, and that this comes from the innermost radii, close to the perturber. The deficit is also present from the very start, and never matches the predicted solution, even at large times. If this deficit were present in a wider physical context, the reduced force would act for a significant amount of time, and would not be disrupted by larger scale differences to the analytic setup. By this, we mean that even if the medium is not isotropic, the force from an induced wake from the local density will still be reduced, since the error comes from these inner parts which will not be changed by large scale variations in the background, or other effects that disrupt the extended parts of the wake.

4.4 Additional Tests

While the setup of these idealised simulations can be parameterised by only two variables, the Mach number and A parameter, it is worth considering if the underlying physical quantities that define these values could be causing the force deficit, which we discuss above. We test our findings by varying these parameters, and the numerical setup of the simulations themselves, namely by varying the spatial and temporal resolutions.

When we look at the definition of the linearity of the problem, through the A parameter, given in Equation 6, we see that it depends on the mass of the perturber M_p , the sound speed of the gas c_s , and the softening scale of the perturber r_s . In our results so far, the different A values have been achieved by varying the perturber mass, and holding all else constant. We now vary the background temperature, by an order of magnitude, to test whether the discrepancies remain at different scales. This effectively changes the sound speed of the gas. To maintain the same A values, the perturber mass is also changed by the corresponding amount. The problem is scale free, so the results should not change with these variations. We find that the evolution of the force from the wake that is generated is unchanged by the varying of these parameters. The same differences between the numerical and analytic solutions are seen with these new conditions.

Testing the convergence of results based on spatial resolution, via the number of particles, using runs GM64M13A01 to GM256M13A1, produces the same evolution whether we use $N = 64^3$, $N = 128^3$, $N = 256^3$, or $N = 512^3$ particles, in effect increasing the spatial resolution from $0.8r_s$ to $0.1r_s$. The bulk velocity and sound speed of these runs are identical, with only the particle mass changing, to maintain the same background density. This force evolution is shown in Figure 12. We have therefore converged with resolution. The exact form of the wake also converges, showing the same structures at $N = 256^3$. At resolutions below this, the resolution is too low to practically assess the shape of the detailed structure of the wake. The Lagrangian nature of the methods used here mean spatial resolution comparisons, to previous works on Eulerian grids, are not simple. The kernel lengths in a typical run are of order $0.1r_s$, compared to 1 cell per r_s (Sánchez-Salcedo & Brandenburg 1999), or 5 cells per r_s and 6 cells per r_s , in KK09 and BS13 respectively. All previous works considered here are run in 2D, while our own work uses full 3D. Similarly, using the GOPSPH solver, in the place of the GOMFM solver, also does not change our findings, so the differences in wake and force evolution are not unique to the GOMFM solver. Another crucial aspect of numerical schemes is the integration time-step. We test if the standard time-

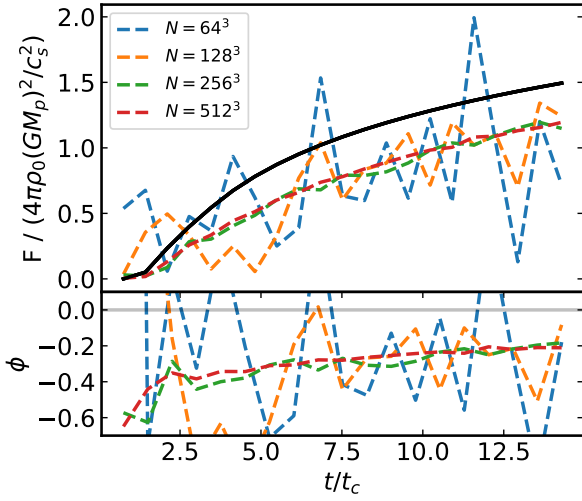


Figure 12. *Upper panel:* Evolution of the dimensionless force, for $A = 0.1$, for different particle numbers, showing $N = 64^3$ (blue), $N = 128^3$ (orange), $N = 256^3$ (green), and $N = 512^3$ (red). The evolution is essentially identical for all resolutions, but with significantly increased random variation for $N = 64^3$ and $N = 128^3$. *Lower panel:* Residual between numerical and analytic wakes $\phi = (F_{\text{num}} - F_{\text{ana}})/F_{\text{ana}}$.

step could be the source of the mismatch by reducing the integration time step, by an order of magnitude. This is achieved by decreasing the maximum time step parameter of the simulation, to which the actual time-step is approximately equal, in this setup. This change does not have any effect on the evolution of the wake.

On top of this, we produced a set of comparison runs using Gadget4 (Springel et al. 2020), listed as 4P512M13A01 and 4P512M13A1. These use identical initial conditions, and an identical simulation setup, to investigate if the force deficit found here is peculiar to GIZMO. Using the G4PSPH solver, we see exactly the same force evolution from both the original GIZMO and new Gadget4 results. This is shown in Figure 13, with the force from the Gadget4 runs shown in blue, and the original GIZMO results in orange. As before, the force evolution from the wake beyond $r = 4r_s$ matches the analytic prediction to within 5%, for $A = 0.1$. The consistency of the results demonstrates that the mismatch is not unique to the hydro-schemes in the GIZMO simulation code.

4.5 Minimum Radius Fit

As we have discussed in Section 4.1, we have found the radius beyond which our numerical results produce a drag force that matches the equivalent analytic force. Specifically, we find that $r_{\text{min}} = 4r_s$ for $A = 0.1$, and $r_{\text{min}} = 8r_s$ for $A = 1$. In this sub-section, we compare the force deficit in our results when we use the various fits described in previous works. The two fits we compare to here are those used in KK09 and BS13, which are $r_{\text{min}} = 0.35M^{0.6}r_s$ and $r_{\text{min}} = 2.25r_s$, respectively. BS13 also investigate a Mach dependent fit, but we do not consider that here. The $r_{\text{min}} = 2.25r_s$ fit is also used by Sánchez-Salcedo & Brandenburg (1999). These fits do not vary with A , and both were found from runs that include ones using $A = 0.01$. In Figure 14, we show the fractional residual between the numerical and analytic forces, using the different fits for r_{min} . The circles show the results using the fits from this work, the triangles use the fit from KK09 and the squares the fit from BS13. The blue results use $A = 0.1$, and the red $A = 1$. This figure shows that the

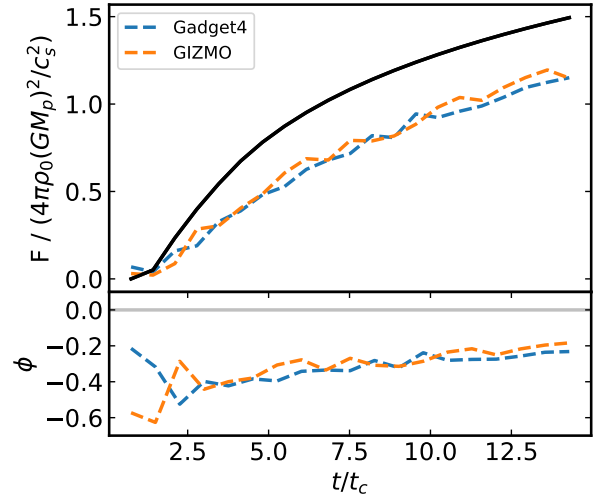


Figure 13. *Upper panel:* Evolution of the dimensionless force, for $A = 0.1$, from the Gadget4 (blue), and GIZMO (orange) results. The evolution is essentially identical. *Lower panel:* Residual between numerical and analytic wakes $\phi = (F_{\text{num}} - F_{\text{ana}})/F_{\text{ana}}$.

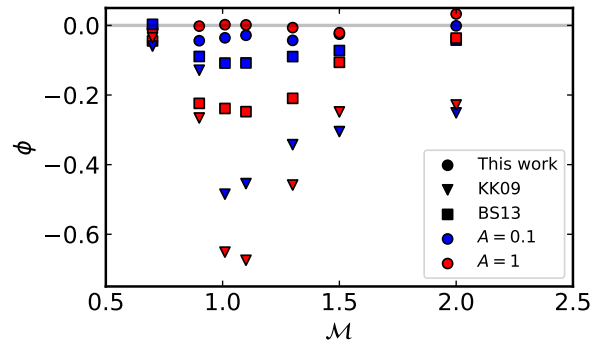


Figure 14. Residual $\phi = (F_{\text{num}} - F_{\text{ana}})/F_{\text{ana}}$, between the numerical and the expected analytic forces, using fits found in this work (circles), KK09 (triangles), and BS13 (squares). Results with $A = 0.1$ shown in blue, $A = 1$ in red.

fits found in previous works do not produce accurate forces from our numerical wakes, for $0.7 < \mathcal{M} < 2.0$. With $\mathcal{M} \leq 0.7$, all fits produce forces that match to within 5% of the prediction. At the other end of the tested range, where $\mathcal{M} \geq 2.0$, all but the KK09 fit produce close matches. This is consistent with our previous results, as both fits produce smaller minimum radii. Our results find that the wake is poorly recovered to a greater distance than previous works, so the previous fits include regions that are poorly recovered in our results.

The fit that we identify here is based on a systematic expansion of the minimum radius of the force integration. The radius at which the fractional residual drops to $\phi \leq 0.01$ is shown in Figure 15. The exact radius at which this happens is not constant with Mach number, so the final fit is an approximation, and only holds for the stated Mach range of $0.7 < \mathcal{M} < 2.0$. There is scatter of order r_s about the mean values shown here. The minimum radii used by previous works are also shown. Some of the Mach number runs do not achieve a match within 1%, so these are not included in the plot. The key result from this figure is the proportion of missing force in our numerical results.

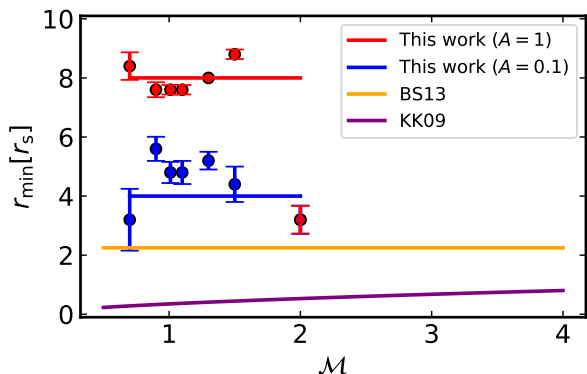


Figure 15. Minimum radius beyond which the force integration of the numerical wake produces a retarding force that is within 1% of the predicted force. Our results for $A = 0.1$ (red dots) and $A = 1$ (blue dots), with the corresponding fits shown as red and blue lines respectively. Error bars are found by taking the standard deviation of the r_{\min} found for the last five snapshots of each run.

It should be noted that we are comparing our full 3D results to results from 2D simulations. These works implicitly assume that their results are rotationally symmetric, as does the analytic solution. In essence, they extrapolate their results from 2D to 3D. In doing so, these works cannot account for variation/fluctuations in the wake that occur in different 2D slices. Our results effectively average over these fluctuations, but they are still present in our final results. The comparisons of our results to theirs is therefore not perfect, but since we both end up with the cylindrical symmetric results, it is adequate for what we do here.

5 DISCUSSION

There are a number of possible numerical causes for the mismatch between these results and the linear predictions. Since both the Lagrangian solvers used here are run using the same gravity backbone, it is possible the gravitational force felt by the gas particles is not replicating the assumptions made in the derivation of the liner solution. We have added the Plummer potential as a fixed external potential, and disabled the self gravity of the gas. The Plummer potential is used to soften the gravitational force felt by particles that pass very close to the origin of the potential, as the potential for a point mass diverges. This can create extreme accelerations, where particles are flung off at great speeds, when particles move unphysically close to the perturber (i.e. when the physical extent of the perturber could overlap with the gas packet represented by the numerical particle). The analytic prediction assumes that the perturber is a point mass, however, the solution for an extended perturber (whose extent is r_{\min}) should be identical to the solution beyond r_s (Ostriker 1999). Additionally, we find, in gravity only runs, that the code reproduces the expected force from a collisionless medium, with an error smaller than the closest matching gaseous case (i.e. $\phi < 0.1$), in the Mach regime we consider here. The analytic solution for this result makes a similar point mass assumption, so the change to the Plummer potential is not the source of the mismatch in the collisional/gaseous case.

Previous numerical studies have also used Plummer potentials, and have recovered the analytic prediction under certain conditions. It should be noted that a key condition is the choice of r_{\min} , and the works find different fits for the r_{\min} value that produces the analytic

force. The fit that we find here shows that these solvers produce a wake that does not match the prediction at small radii, and that the mismatch extends significantly further than previous works have found. Consequently, we show a significant force deficit from the physical drag force, where previous works do not. It is possible that the use of this gravitational softening means that particles that pass close to the perturber are feeling the incorrect force. Their trajectories, even once they have moved beyond the softening length, will not be completely physically correct. This does not explain the bow structure, however, which extend more than r_s ahead of the perturber, nor the lower density peak in the cone profile at a few r_s from the perturber, where the vast majority of the particles will not have passed close to the perturber.

The problem may lie with recovering the hydrodynamics itself, rather than the gravitational force. The solvers used here are Lagrangian in nature, while the major numerical studies we refer to are performed using Eulerian grid based methods. Particle based methods have traditionally struggled to capture sharp changes in density, which we see in the density profile of the cone front. It is possible that the smearing out of this profile leads to the development of the density ahead of the perturber, as the over-density spreads ahead of its predicted position. The combination of the smeared profile and bow structure produce the difference in the net force on the perturber, and it is possible that they are an artifact of the Lagrangian nature of the solver. The profile is spread over 10 – 20 times the typical kernel length of the simulation, so the solver should be able to resolve much sharper structure within this region.

We see that the problem gets worse as we move from $A = 0.1$ to $A = 1$. At this greater A value, we are at the edge of the regime that the analytic solution covers, but we should still be able to recover the expected structure. The structure we do find is somewhat reminiscent of that described for the extreme non-linear cases in KK09 and BS13, but it should not be present at this linearity. Since we see that the force also does not match at $A = 0.1$, and that the force from the $A = 0.01$ case is essentially identical to that from $A = 0.1$ (see Figure 3), it is safe to assume the problem is not simply caused by the break down of the analytic solution, but is instead caused by the numerical method.

5.1 Implications for Cosmological Simulations

We have shown that there is a significant DF force deficit, across many crossing times, when idealised dynamical friction tests are run using Lagrangian hydrodynamics solvers, such as MFM and PSPH. This force deficit is caused by the over-dense wake being improperly formed. These Lagrangian solvers do not reproduce the sharp edge of Mach cone predicted by the analytic work, and the conditions continue for at least $t = 150t_c$. Here we discuss the implications this has for DM substructure in cosmological simulations.

The typical conditions in which we find sub-haloes in cosmological simulations can be mapped onto this idealised setup by estimating the appropriate Mach number and A parameter. We have taken the simulations results from the IllustrisTNG-300 public data (Nelson et al. 2019), using the halo and sub-halo catalogues at $z = 0$. We select all host haloes in the mass range $M_p = 10^{11} M_\odot$ to $10^{15} M_\odot$. The distribution of masses and sound speeds for all sub-haloes are shown in Figure 16. The top plot shows the conditional probability of a sound speed, given a sub-halo mass. The sound speed is only dependent on the mass of the host (see Appendix B), which leads to the bands at the high sound speed/host mass end,

where there are the fewest samples. We effectively see the negative slope in the power law distribution of halo/sub-halo masses, as there are many more sub-haloes associated with low mass haloes (low sound speeds), even though the most massive haloes individually contain many more sub-haloes than any given lower mass halo. The middle plot shows the mean Mach number for each pixel. The distribution is fairly uniform across both mass and sound speed. The mean Mach number is around $\mathcal{M} = 1 - 2$. This is also shown in the top panel of Figure 17 with the conditional probability of a Mach number, given a sub-halo mass. The bottom plot of Figure 16 shows the mean A parameter for each pixel. The distribution at the high sub-halo mass end is dominated by small numbers of very high A parameter values in each cell. The overall distribution of A parameters is shown in the middle panel of Figure 17. The distribution has been truncated at $A = 10$, but continues to values in the thousands. We show the conditional probability of finding an A number, given a sub-halo mass. The sub-haloes below $M_p = 10^{10} M_\odot$ in mass exist well within the linear regime ($A \ll 1$). Those between $M_p = 10^{10} M_\odot$ and $10^{11} M_\odot$ show a wider range of A , numbers but still mostly reside in the linear or quasi linear regime ($A \leq 1$). Above this mass, the distribution spreads significantly, with a range of A numbers, a significant fraction in the non-linear regime ($A > 1$).

The IllustrisTNG-300 sub-haloes show that a large fraction of sub-haloes in a typical state-of-the-art cosmological simulation exist within the linear DF regime, with $A < 1$, and with Mach numbers in the range $\mathcal{M} = 1 - 2$. This is the regime in which we have found a discrepancy between the analytic prediction, previously confirmed by previous high resolution simulations, and the numerical results from these solvers. The bottom panel of Figure 17 show the distribution of sound speed crossing times for the radial extents of these sub-haloes. We see that these values are of order $10 - 100$ Myrs. The period for which we have found significant divergence from the analytic solution is at a minimum $15t_c$, with some results extending up to at least $150t_c$. The force would therefore be missing for at least hundreds of mega-years, and since likely longer. The numerical results from the previous Eulerian works find a long time until the solution has converged to the predicted result, as such as $300 - 600t_c$ (Kim & Kim 2009), so this problem may exist across other hydro methods. The reduced force for extended periods of time will lead to significantly slower infall of sub-haloes into their host structure. The energy and angular momentum transferred from the perturbing sub-halo to the CGM will be equally reduced.

A number of factors make DF in a system with more complete physical processes diverge from the analytic solution. The gas will obviously experience self gravity, leading to the further growth of the over-dense wake. Radiative cooling mechanisms move the gas away from the adiabatic scenario considered in the analytic solution. Feedback mechanisms from star formation, such as supernova driven winds, will also have complex effects. These will all be present in the full cosmological context of cosmological simulations. The effect of these processes will be to significantly change the structure of the wake in complex ways. However the fundamental mechanism of the problem is still present, since any structure that physically should remain will likely underestimate the DF force in the same way as found in the simplified case. The numerical DF force will then still undershoot the physically correct DF force. We plan to run a set of simulations that will probe the effects of self gravity and radiative cooling in the development of the wake, in the light of these results.

While we have assumed, in our idealised setup, that the background medium has a uniform density, the simulated medium through which the sub-haloes move will be far from uniform. The

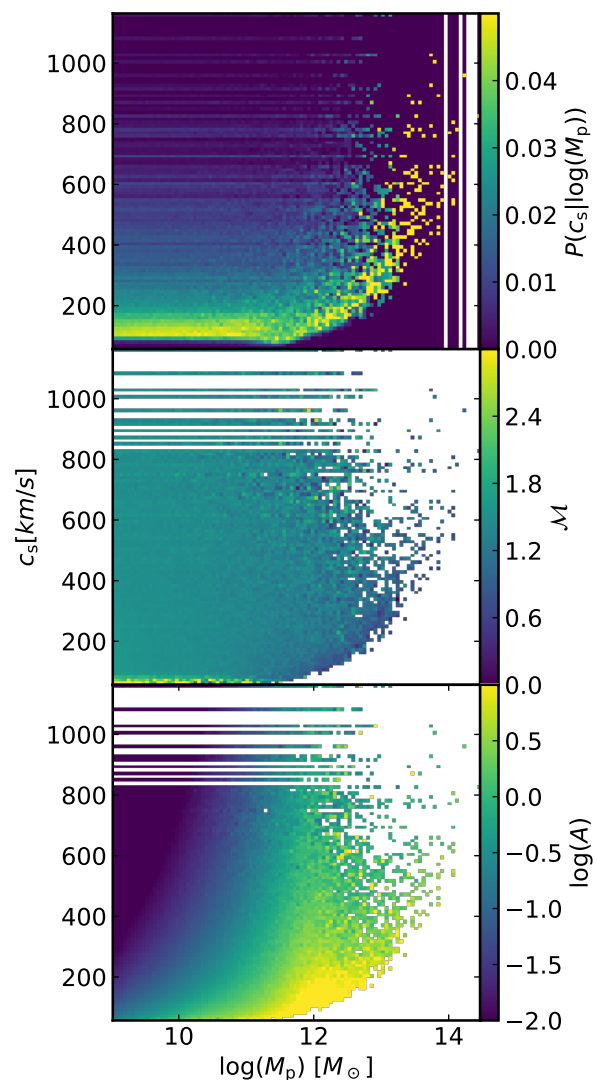


Figure 16. Sub-haloes from the IllustrisTNG-300 simulation box at $z = 0$. Sound speeds are calculated from the virial temperature of the host halo, dependent on the virial mass M_{200} . All panels show the sub-haloes with masses between $M_p = 1 \times 10^{11} M_\odot$ and $1 \times 10^{15} M_\odot$, binned into sub-halo mass - sound speed pixels. *Top panel:* The colour in this panel indicates the conditional probability of finding a sound speed, given a certain sub-halo mass. *Middle panel:* Average Mach number of the sub-haloes in each (M_p, c_s) pixel. The sub-halo velocity is taken as the peculiar velocity of the sub-halo, relative to the velocity of the host halo. *Bottom panel:* Average A value in each (M_p, c_s) pixel. The softening scale equivalent radius is taken to be the radius of the max velocity, based on the density profile of the sub-halo.

CGM is highly variable, made up of gas with a huge range of sound speeds. The wake will not build up smoothly as shown in the idealised scenario, where it can grow for an unlimited time through an infinite uniform background medium. Instead, at any given time, the wake will be built from the medium that the perturber (sub-halo) is moving through at that time. In the context of results, however, this is not that significant, since the DF force deficit that we find comes from the inner most radii, and starts from the earliest time. The wake further from the perturber does not contribute to the missing force, so whether it is present, or disrupted by the more complex physical conditions of the medium, the force deficit will still be present. Thus

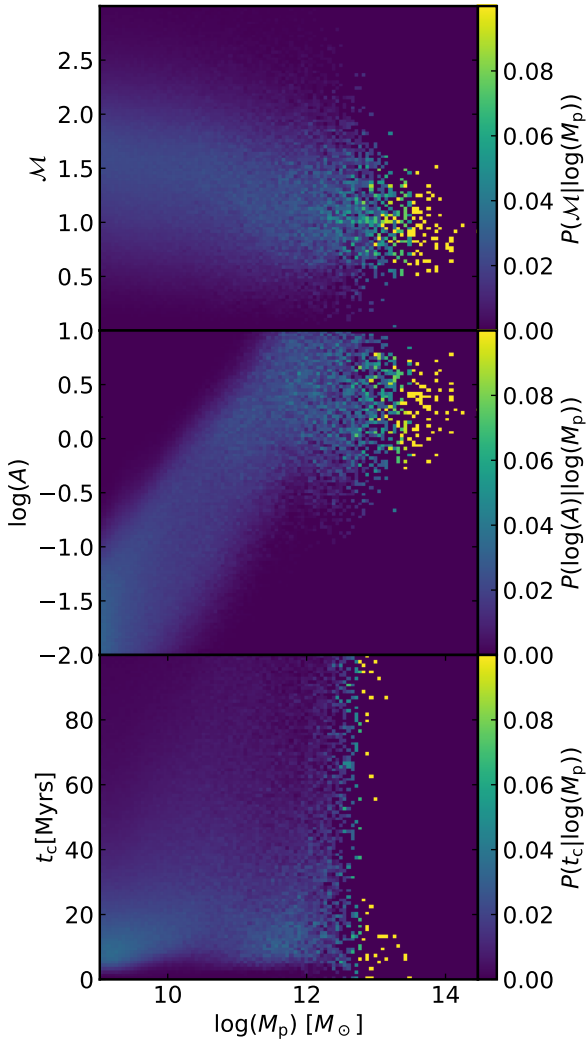


Figure 17. *Top panel:* Conditional probability of finding a Mach number, given a subhalo mass. The majority of sub-haloes have mach numbers in the $\mathcal{M} = 1 - 2$ range. *Middle panel:* Conditional probability of finding an A number, given a sub-halo mass. sub-haloes with masses below $10^{10} M_{\odot}$ all exist well within the linear regime ($A \ll 1$). Above this mass, a significant fraction in each mass bin are either in the transition regime, or into the non-linear regime. *Bottom panel:* Conditional probability of finding a crossing time, given a sub-halo mass. This crossing time is defined as the sound speed crossing time of the radial extent of the sub-halo. For sub-haloes of mass $10^9 M_{\odot}$ to $10^{12} M_{\odot}$ there is large spread of crossing times, with broad peak at $t_c = 10 - 30$ Myrs.

this result has implications far beyond the highly idealised scenario studied directly here, into the cases that include more varied and complex physical processes.

5.2 Gaseous DF as a Standard Grav-Hydro Test

As we have seen in the preceding sections, the idealised gaseous dynamical friction problem presents a tough challenge for modern gravo-hydrodynamical solvers. It combines both gravitational forces and fluid dynamics, and includes complex flows which will not be aligned with any underlying structured mesh. The presence of the Mach cone, with its sharp density profile, one which is not aligned directly with, or orthogonal to, the bulk flow is a particular

challenge. These factors make this setup an ideal candidate for a new standard numerical test case for multi-physics astronomical codes. The problem has a well defined analytic prediction, for both the structure of the over-dense wake, and the force produced by that wake. This allows for direct assessment of the accuracy of the numerical results, something that is relatively rare for tests that include complex, multi-dimensional fluid flows, one which include the effects of both fluid and gravitational forces. The process of DF is also present across a range of important astrophysical problems, and is a critical part of many of them, so understanding the abilities of our numerical methods in this area is important for our wider understanding of the underlying physics of these systems.

An additional strength of this problem, as a standardised test, is its scale free nature. Any setup of the problem can be exactly defined by only two parameters, the A value, which effectively defines the linearity of the problem, and the Mach number \mathcal{M} . Any combination of sound speed, perturber mass, and potential softening can be compared through these scale free parameters. The only limit in comparing to the analytic solution is that of linearity. In other words, the analytic solution assumes the wake is linear at all positions used in the comparison, such that the comparison is best made at $A < 1$. It is therefore extremely easy to directly compare multiple sets of numerical results to the analytic prediction, and to one another. For instance, reproducing plots such as that shown in Figure 2, compares results across A and \mathcal{M} to the analytic solution.

We propose this setup of a massive perturber, represented by some softened fixed potential, embedded within a gaseous medium moving with some bulk flow, be used as a standard test for current and new multi-physics codes. It concisely assesses the accuracy of both hydrodynamic and gravity solvers, used in conjunction, with a well defined solution, but one which is a challenge to reproduce. In particular, using results close to $\mathcal{M} = 1$, where the gaseous response is most pronounced, and the drag force is greatest, will produce interesting comparisons.

6 CONCLUSIONS

We have shown that a class of Lagrangian hydrodynamical solvers widely used in astrophysics produce over-dense wakes, from a massive perturber, that do not match the wake predicted by linear perturbation theory. Instead, the numerical wakes produce a force that is between 10% and 50% below that predicted by the analytic treatment (see Figure 2). This significant difference is present across $\mathcal{M} \sim 1 - 2$, to at least $150r_c$. The largest difference is found close to $\mathcal{M} = 1$, with cases at $\mathcal{M} = 0.7$ and $\mathcal{M} = 2$ showing agreement to within 5% of the predicted force. The deficit is present well within the linear regime, shown in Figure 3 to be present down to at least $A = 0.01$. We see in Figure 6 that the wake, in the innermost regions, does not match the predicted over-dense structure. A bow-shock like structure builds up in front of, and to either side of, the perturber, while the sharp profile in the over-density of the Mach cone is smeared out. The front is smoothed out and the peak in the over-density is lowered. This softening extends along the cone front, but the largest impact on the force comes from differences in the innermost $4r_s$ (for $A = 0.1$) or $8r_s$ (for $A = 1$). The evolution of the force in the innermost regions shows extreme divergence early on, when the wake barely extend beyond the softening scale of the potential, but soon converges to a quasi-steady form. Spherical shells further from the perturber show no similar trend, showing that the wake at that distance has the predicted structure, for all times that it extends into that shell. The evolution of the force is identical for

tests with the alternative G4PSPH solver, and with varied initial conditions.

The missing force is caused by the unphysical development of the gravitationally induced wake. The over-density along the leading edge of the Mach cone is smeared out, with material further forward than predicted. The sharp profile is smeared out, and the over-dense wake projects ahead of the perturber itself. Together these mean that the wake produces a lower drag force. The inaccuracy extends to a number of radii, $4r_s$ in the $A = 0.1$ case, and $8r_s$ with $A = 1$. Beyond these radii, the respective wakes produce forces that match the expected force, to within at least 5% of that expected force.

A significant proportion of cosmological dark matter substructure is found in the regimes that show the most force deficit. Any DF that these structures should experience will not be well recovered in these large scale simulations. Merger rates of these structures will therefore be underestimated in these simulations, leading to incorrect halo masses and merger histories.

It is clear that DF is a complex problem for modern hydro solvers to treat. We have shown that state-of-art solvers can struggle to replicate the analytic solution. DF as a process that is present in astrophysical systems across a host of mass and length scales, and is crucial to our understanding of the evolution of these systems. This makes DF an ideal candidate for inclusion as a standard test when developing numerical hydrodynamics methods and algorithms. It has a well defined solution for comparison, and includes both a shock with complex geometry and regions with simpler advective flows. The scale free nature of its formulation, with the A parameter and Mach number as the defining variables, allow for straight forward comparison between numerical tests.

ACKNOWLEDGEMENTS

This work was performed using the Cambridge Service for Data Driven Discovery (CSD3), part of which is operated by the University of Cambridge Research Computing on behalf of the STFC DiRAC HPC Facility (www.dirac.ac.uk). The DiRAC component of CSD3 was funded by BEIS capital funding via STFC capital grants ST/P002307/1 and ST/R002452/1 and STFC operations grant ST/R00689X/1. DiRAC is part of the National e-Infrastructure.

We acknowledge that the results of this research have been achieved using the DECI resource ARCHER based in the UK at EPCC with support from the PRACE aisbl.

This work also used the Cirrus UK National Tier-2 HPC Service at EPCC (<http://www.cirrus.ac.uk>) funded by the University of Edinburgh and EPSRC (EP/P020267/1).

DATA AVAILABILITY

All data produced from the simulations discussed in this work are available on request.

REFERENCES

- Adhikari S., Dalal N., Clampitt J., 2016, *J. Cosmology Astropart. Phys.*, **2016**, 022
- Agertz O., et al., 2007, *MNRAS*, **380**, 963
- Arth A., Donnert J., Steinwandel U., Böss L., Halbesma T., Pütz M., Hubber D., Dolag K., 2019, arXiv e-prints, p. [arXiv:1907.11250](https://arxiv.org/abs/1907.11250)
- Barnes J. E., Hernquist L., 1996, *ApJ*, **471**, 115

- Beckman J., Carretero C., Vazdekis A., 2008, *Chinese Journal of Astronomy and Astrophysics Supplement*, **8**, 77
- Beckmann R. S., Slyz A., Devriendt J., 2018, *MNRAS*, **478**, 995
- Bernal C. G., Sánchez-Salcedo F. J., 2013, *ApJ*, **775**, 72
- Bonetti M., Bortolas E., Lupi A., Dotti M., Raimundo S. I., 2020, *MNRAS*, **494**, 3053
- Bortolas E., Bonetti M., Dotti M., Lupi A., Capelo P. R., Mayer L., Sesana A., 2021, arXiv e-prints, p. [arXiv:2103.07486](https://arxiv.org/abs/2103.07486)
- Boylan-Kolchin M., Ma C.-P., Quataert E., 2008, *MNRAS*, **383**, 93
- Bryan G. L., et al., 2014, *ApJS*, **211**, 19
- Chandrasekhar S., 1943, *ApJ*, **97**, 255
- Daddi E., et al., 2010, *ApJ*, **714**, L118
- Donnert J. M. F., Beck A. M., Dolag K., Röttgering H. J. A., 2017, *MNRAS*, **471**, 4587
- Dosopoulou F., Antonini F., 2017, *ApJ*, **840**, 31
- Duffell P. C., 2016, *ApJS*, **226**, 2
- Duffell P. C., MacFadyen A. I., 2011, *ApJS*, **197**, 15
- El-Zant A. A., Kim W.-T., Kamionkowski M., 2004, *MNRAS*, **354**, 169
- Fujii M., Funato Y., Makino J., 2006, *PASJ*, **58**, 743
- Gingold R. A., Monaghan J. J., 1977, *MNRAS*, **181**, 375
- Gonnet P., 2014, arXiv e-prints, p. [arXiv:1404.2303](https://arxiv.org/abs/1404.2303)
- Hopkins P. F., 2013, *MNRAS*, **428**, 2840
- Hopkins P. F., 2015, *MNRAS*, **450**, 53
- Just A., Kegel W. H., 1990, *A&A*, **232**, 447
- Just A., Khan F. M., Berczik P., Ernst A., Spurzem R., 2010, *MNRAS*, **411**, 653
- Khochfar S., Ostriker J. P., 2008, *ApJ*, **680**, 54
- Khochfar S., et al., 2011, *MNRAS*, **417**, 845
- Kim H., Kim W., 2007, *ApJ*, **665**, 432
- Kim H., Kim W.-T., 2009, *ApJ*, **703**, 1278
- Kim W.-T., El-Zant A. A., Kamionkowski M., 2005, *ApJ*, **632**, 157
- Ma L., Hopkins P. F., Ma X., Anglés-Alcázar D., Faucher-Giguère C.-A., Kelley L. Z., 2021, arXiv e-prints, p. [arXiv:2101.02727](https://arxiv.org/abs/2101.02727)
- Menon H., Wesolowski L., Zheng G., Jetley P., Kale L., Quinn T., Governato F., 2015, *Computational Astrophysics and Cosmology*, **2**, 1
- Namouni F., 2010, *MNRAS*, **401**, 319
- Nelson D., et al., 2019, *Computational Astrophysics and Cosmology*, **6**, 2
- Ogiya G., Burkert A., 2016, *MNRAS*, **457**, 2164
- Ostriker E. C., 1999, *ApJ*, **513**, 252
- Plummer H. C., 1911, *MNRAS*, **71**, 460
- Robaina A. R., Bell E. F., van der Wel A., Somerville R. S., Skelton R. E., McIntosh D. H., Meisenheimer K., Wolf C., 2010, *ApJ*, **719**, 844
- Sánchez-Salcedo F. J., Brandenburg A., 1999, *ApJ*, **522**, L35
- Sánchez-Salcedo F. J., Brandenburg A., 2001, *MNRAS*, **322**, 67
- Somerville R. S., Davé R., 2015, *ARA&A*, **53**, 51
- Springel V., 2005, *MNRAS*, **364**, 1105
- Springel V., 2010, *MNRAS*, **401**, 791
- Springel V., et al., 2008, *MNRAS*, **391**, 1685
- Springel V., Pakmor R., Zier O., Reinecke M., 2020, arXiv e-prints, p. [arXiv:2010.03567](https://arxiv.org/abs/2010.03567)
- Tacconi L. J., et al., 2010, *Nature*, **463**, 781
- Tagawa H., Saitoh T. R., Kocsis B., 2018, *Phys. Rev. Lett.*, **120**, 261101
- Teyssandier J., Terquem C., Papaloizou J. C. B., 2012, *MNRAS*, **428**, 658
- Thun D., Kuiper R., Schmidt F., Kley W., 2016, *A&A*, **589**, A10
- Tittley E. R., Pearce F. R., Couchman H. M. P., 2001, *ApJ*, **561**, 69
- Toyouchi D., Hosokawa T., Sugimura K., Kuiper R., 2020, *MNRAS*, **496**, 1909
- Wadsley J. W., Stadel J., Quinn T., 2004, *New Astron.*, **9**, 137
- Wadsley J. W., Keller B. W., Quinn T. R., 2017, *MNRAS*, **471**, 2357
- Weisz D., Boylan-Kolchin M., 2019, *BAAS*, **51**, 1
- Zhao H., 2004, *MNRAS*, **351**, 891

APPENDIX A: INTRINSIC FORCE VARIATION

The A parameter, which effectively sets the linearity of the numerical setup, can be varied by changing any of its dependent variables:

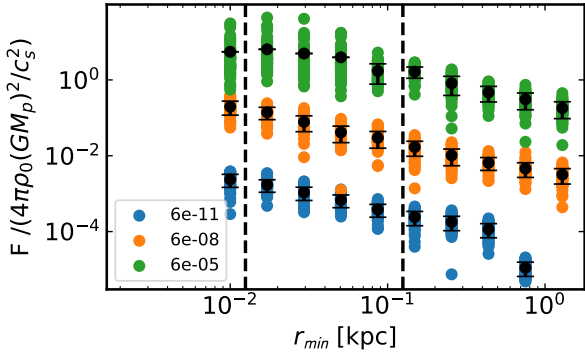


Figure A1. Force on a $M_p = 2.5 \times 10^3 M_\odot$ perturber from the initial particle distribution for setups with mass ratios of $M_{\text{particle}}/M_{\text{perturber}} = 6 \times 10^{-11}$ (light blue dots), 6×10^{-8} (orange dots), 6×10^{-5} (green dots). ICs are randomly shifted 50 times for each tested r_{min} . The coloured dots show the net dimensionless force on the perturber at the centre of the box, excluding all particles within r_{min} of the perturber. The black dots show the mean force at that r_{min} , with error bars showing the standard deviation in the forces. The variation rises significantly with particle-perturber mass ratio, and falls as r_{min} is increased. The variation shown here effectively limits the scenarios that can be run with these solvers.

the perturber mass, the sound speed of the background gas, and the gravitational softening scale of the perturber. Setups with the same A parameter constructed with different combinations of these parameters should produce the same results. However, there is an intrinsic error in the force produced by a given setup, effectively dictated by the inner radius, which forms the lower limit of the force integral, the mass of the perturber, and the mass of the gas particles. If we consider a scenario where the perturber does not act on the medium, then as the initial distribution of particles moves past the perturber position, the configuration of finite masses will produce variation in the net force on the perturber. This force from the unperturbed medium should be zero, but the sampling of the medium by finite mass particles leads to some variation from this value. The lower limit of the integral sets the distance of the nearest particle included in the force summation. Small lower limits lead to large contributions from the particles very close to the perturber, where the small volumes are sampled by few particles. Large r_{min} leads to smaller variation. For a given background density and integral lower limit, the ratio of the particle mass to perturber mass M_{part}/M_p has a significant role in determining the level of intrinsic variation. The larger this ratio is, the more severe the impact of the closest particles to the perturber. Figure A1 shows the force on the central massive perturber from the glass like initial conditions. The force was calculated by direct summation of the Newtonian gravitational force between the central mass and the gas particles, excluding particles within r_{min} of the centre. This effectively shows the uncertainty in the force for different choices of the inner radius. The specific cases shown here are for the $M_p = 2.5 \times 10^3 M_\odot$ perturber and $N = 512^3$ particles, with $L = 1, 10, 100$ kpc. The ratios of particle mass to perturber mass are 6×10^{-11} (light blue), 6×10^{-8} (orange), and 6×10^{-5} (green) respectively.

The numerical dimensionless force increases linearly with the ratio of particle mass to perturber mass, for a given background density. We can estimate the underlying uncertainty in the force from the output of a given setup. This intrinsic variation effectively limits the setups that will produce useful results, because the error can be too large to say anything meaningful about the force from the resultant wake. We must balance the need for a large box to reach

large numbers of crossing times with the need to keep the number density high.

APPENDIX B: SIMULATION DATA

We are using haloes and sub-haloes from the IllustrisTNG-300 simulation box (Nelson et al. 2019), at redshift $z = 0$, to assess the conditions in which simulated sub-haloes are found. We select all host haloes in the mass range $10^{11} M_\odot$ to $10^{15} M_\odot$. For each host in this range, we then assign a sound speed. This sound speed is calculated from the virial temperature of that halo

$$c_s = \sqrt{\frac{\gamma k_B T_{\text{vir}}}{\mu m_p}}, \quad (\text{B1})$$

where μ is the mean molecular weight of the gas, m_p is the mass of a proton. The virial temperature T_{vir} is found by assuming that the gas falling onto the virial radius transforms its kinetic energy into thermal energy. If we assume this produces an isothermal sphere, the virial temperature is given by

$$T_{\text{vir}} = \frac{1}{3} \frac{\mu m_p}{k_B} \frac{GM_{200}}{r_{200}}. \quad (\text{B2})$$

The virial mass is taken as the mass M_{200} enclosed within the radius r_{200} . This is the radius at which the the average density of the enclosed material falls to two hundred times the critical density ρ_{crit} . The sub-haloes associated with these hosts are then binned by their mass and this sound speed. The most massive sub-halo in each host is excluded, as it is assumed to be the central object of that halo.

These sub-haloes are taken as the perturbing massive objects, as they move through the extended gaseous medium of their host. The peculiar velocity of the sub-halo, relative to the peculiar velocity of the host halo, defines the velocity for the calculation of the sub-halo's Mach number. The radial extent of the sub-halo is the equivalent to the softening scale of the Plummer potential. This is taken as the radius at which the density profile of the sub-halo produces the maximum circular velocity V_{max} . The mass of the sub-halo, which is the equivalent quantity to the mass of the perturber, is simply the total baryonic and dark matter mass associated to that sub-halo by the halo identification algorithm.

This paper has been typeset from a \LaTeX file prepared by the author.